AIAA 97-0556

Disturbance Evolution and Breakdown to Turbulence in a Hypersonic Boundary Layer: Instantaneous Structure

J. Poggie and R. L. Kimmel
Wright Laboratory
Wright-Patterson AFB, OH

35th Aerospace Sciences Meeting & Exhibit
January 6-10, 1997 / Reno, NV

DISTURBANCE EVOLUTION AND BREAKDOWN TO TURBULENCE IN A HYPERSONIC BOUNDARY LAYER: INSTANTANEOUS STRUCTURE

J. Poggie*
R. L. Kimmel†

USAF Wright Laboratory‡
WPAFB, OH

January 8, 1996

Abstract

Preliminary results are presented of a study of the instantaneous structure of disturbances in a hypersonic boundary layer. The experimental data suggest that the flow is dominated by two-dimensional second mode instability waves; no evidence of skewed first mode waves was found.

1 Introduction

Wave packets appear to be a universal feature of 'natural' transition in a relatively low-disturbance environment. For a low-speed, flat-plate boundary layer flow, for example, the oscillograms presented in the famous experiments of Schubauer and Skramstadt [1] show a low-level signal alternating intermittently with high-amplitude 'bursts.' At the opposite end of Mach number range, Potter and Whitfield [2] observed packets of 'rope waves' in schlieren photographs of a hypersonic flow over a cone.

A number of researchers have examined a simplified wave packet problem, in which a short, localized pulse is introduced into a laminar boundary layer flow (e.g., see References [3, 4, 5, 6]). The resulting wave packet is studied as it travels downstream in the boundary layer. A short input pulse has a very broad and flat spectrum in frequency-wavenumber space, so all unstable modes tend to be excited evenly. After the transient component dies out, the wave packet takes on an asymptotic form that is independent of the initial conditions. In incompressible boundary layers, this form appears as a corrugated, kidney-shaped patch [3, 7].

A complication arises for wave packets in a hypersonic boundary layer: linear stability theory has identified two important unstable modes that are distinquished by their characteristic functions, or profiles along the wall-normal direction [8]. The first mode is the compressible flow counterpart of the Tollmien-Schlichting wave, and is usually described as vortical in nature. The second (Mack) mode has no counterpart in incompressible flow, and is often described as acoustical in nature. Linear stability theory also predicts that the most unstable first mode disturbance becomes increasingly skewed to the freestream direction as the Mach number increases from zero to the supersonic range, but that the most unstable second mode disturbance is oriented normal to the freestream.

As a disturbance of constant frequency travels downstream through increasing values of the Reynolds number, a skewed first mode component is initially most amplified, and later a two-dimensional second mode component is most amplified (see the discussion in Pruett and Chang [9]). This result suggests that the development of a wave packet in a hypersonic boundary layer is significantly different from the analogous problem in incompressible flow, and that the asymptotic form of the wave packet is a strong function of Mach number and the streamwise station where the disturbance originates.

Further, the phenomenon of transition, in contrast to stability, depends on the total growth of boundary layer disturbances. Point disturbances are introduced randomly all over the boundary layer, and transition is caused by the flow that results from a sum over the histories of all the resulting wave packets (e.g., see Mack [10], p. 3-27).

*Aerospace Engineer, Member AIAA
†Aerospace Engineer, Senior Member AIAA

1.1 Kinematic Approach

A kinematic approach to the study of boundary layer disturbances is of interest because of the complexity of the dynamics of the transition process. Boundary layer transition data can be difficult to interpret in terms of normal modes when the disturbances are in the form of wave packets or when they grow into the nonlinear regime. Important kinematic features include the frequency of occurance of the packets, as well as their length scale, lifetime, orientation, and velocity. Valuable data for transition modelling can be obtained by tracking the changes in these features from the initial onset of instability, through the formation of Emmons spots, to the development of the organized structures observed in fully developed turbulent boundary layers.

A kinematic approach to describing wave motion was developed independently by Landau and Lifshitz [11] and Whitham [12]. This approach generalizes the idea of a travelling plane wave to a slowly-varying, quasi-planar wave train. A wave train Ψ is assumed to have the form:

$$\Psi(\vec{x},t) = A(\vec{x},t)\cos\phi(\vec{x},t) \tag{1}$$

where A is the amplitude function and ϕ is the phase function.

The basic assumption is that, over space and time scales corresponding to one cycle of $\cos\phi$, the amplitude function A is approximately constant and the phase function ϕ is nearly linear. (See Segel [13] for a more precise statement of this restriction.) In consequence, the extrema of the wave train Ψ (the crests and troughs) coincide approximately with extrema of $\cos\phi$, so that lines of constant phase can be associated with wavefronts.

The angular frequency is defined to be the rate of decrease of the phase function with time ($\omega = -\partial\phi/\partial t$), while the wavenumber vector is defined as the gradient of the phase function ($\vec{k} = \nabla\phi$). Since the amplitude A has been assumed to be a slowly-varying function, the quantity $\omega/(2\pi)$, which represents the instantaneous rate at which cycles of $\cos\phi$ cross a given point, can be interpreted as the instantaneous rate that waves cross that point. Similarly, $k/(2\pi)$ can be interpreted as a local measure of the number of waves per unit length along the direction normal to a wave front.

The speed of a crest or trough identified with a particular value of the phase can be determined by taking the time derivative of the equation $\phi(\vec{x},t) = \text{const}$:

$$\frac{d\phi}{dt} = \frac{\partial\phi}{\partial t} + \frac{d\vec{x}}{dt}\cdot\nabla\phi = 0 \tag{2}$$

where $\vec{x}(t)$ describes the trajectory of a point on the iso-phase surface, and $\vec{v} = d\vec{x}/dt$ is its velocity. Using the definition of the unit normal to the surface ($\vec{n} = \nabla\phi/|\nabla\phi|$), we get an expression fixing the normal component of the velocity:

$$\vec{v}\cdot\vec{n} = \frac{-\partial\phi/\partial t}{|\nabla\phi|} = \omega/k \tag{3}$$

Thus, an observer moving at a velocity with a component normal to the iso-phase surface equal to ω/k sees a constant phase. The component of the observer's velocity tangential to the iso-phase surface is arbitrary – wave motion parallel to the wavefront cannot be detected. Thus we define the phase velocity as $\vec{v}_p = (\omega/k)\vec{n}$, which is the velocity of the iso-phase surface normal to itself.

If we add the time derivative of the wavenumber vector to the gradient of the angular frequency we can derive an equation relating the two quantities.

$$\frac{\partial\vec{k}}{\partial t} + \nabla\omega = 0 \tag{4}$$

Under the assumption of nearly-planar waves, Equation (4) can be interpreted as an expression of wave conservation. To see this result, we integrate Equation (4) between two points $\vec{x}_0$ and $\vec{x}_1$ over a path C, and divide by 2π.

$$\frac{\partial}{\partial t}\int_C \frac{\vec{k}}{2\pi}\cdot d\vec{r} = \frac{\omega(\vec{x}_0)}{2\pi} - \frac{\omega(\vec{x}_1)}{2\pi} \tag{5}$$

The term on the left-hand-side represents the time rate of change of the total number of cycles of $\cos\phi$ over the path of integration. The terms on the right-hand-side represent the difference in rates at which cycles of $\cos\phi$ cross the points $\vec{x}_0$ and $\vec{x}_1$. Thus, under the nearly-planar wave assumption, the equation can be interpreted as follows: the rate of change of the number of waves along C is equal to the rate at which waves enter at $\vec{x}_0$ minus the rate at which waves leave at $\vec{x}_1$. In other words, quasi-planar waves retain their identity as they travel.

If the group velocity is defined as $\vec{v}_g = \partial\omega/\partial\vec{k}$, and we take the scalar product of the group velocity with Equation (4), we get:

$$\frac{d\omega}{dt} = \frac{\partial\omega}{\partial t} + \vec{v}_g\cdot\nabla\omega = 0 \tag{6}$$

implying that an observer moving with the group velocity sees a constant frequency. An analogous equation for the wave number vector can be derived if $\omega = f(\vec{k})$, otherwise (e.g., $\omega = f(\vec{k},\vec{x})$) the wavenumber vector changes for an observer moving with the group velocity.

The quasi-planar wave assumption seems to be consistent with experimental observations of boundary layer disturbances upstream of the breakdown to turbulence. Boundary layer properties typically vary slowly in the direction of propagation of a disturbance, and experimental data seem to be consistent with a nearly constant

amplitude and approximately linear phase. Many flow visualization experiments show convincing wave trains (e.g., see Van Dyke [14], the schlieren photographs in Kendall [15], or the beautiful photograph of a wave packet in Benjamin [16]). Thus, the kinematic theory of wave motion is applicable to disturbances in transitional boundary layers, and can be used to define a number of parameters describing experimental measurements of wave packets. In particular, the frequency, wavenumber, phase velocity, group velocity, and wave identity are well-defined in the context of the kinematic wave theory, without reference to the underlying dynamics that cause the wave motion.

1.2 The Present Project

Here we present initial results in a program of research on the intermittent, wave packet character of the flow over a 7° half-angle cone at a freestream Mach number of 8. Detailed measurements with multiple hot-film probes were made by Kimmel [17] across a range of Reynolds numbers from the onset of instability in the laminar boundary layer to nearly the fully turbulent state. Stability theory indicates that the second mode is the dominant instability at this Mach number [8].

The first part of the present report [18] investigates the structure of the boundary layer disturbances in an ensemble-averaged sense, while this part of the work emphasizes the instantaneous structure. The aim of both aspects of the data analysis is to characterize the disturbances in the boundary layer, particularly with regard to their speed, length scale, and orientation. A physical understanding of this aspect of transition will aid the development of improved models of the transition process, and may help to improve estimates of the increase in thermal and fatigue loading associated with transition.

2 Experimental Procedure

The experiments were carried out in the von Kármán Gas Dynamics Facility (VKGDF) Tunnel B at the Arnold Engineering Development Center (AEDC). Tunnel B, which is documented in detail in Reference [19], is a closed-circuit, continuous-run facility with a 1.27 m diameter test section. Incoming air is heated with a natural gas combustion heater, and the tunnel itself is cooled with external water jackets.

The facility is equipped with two axisymmetric nozzles that allow the tunnel to be run at a nominal Mach number of either 6 or 8. At Mach 6, the tunnel can be run with a stagnation pressure in the range of 0.14 MPa to 2.07 MPa, and at Mach 8, between 0.35 MPa and 6.21 MPa. The present tests were carried out at a measured freestream Mach number of $\mathrm{Ma}_\infty = 7.93$, and a stagnation temperature of $T_0 = 728$ K in the settling chamber. Unit Reynolds numbers in the wind tunnel freestream between $U_\infty/\nu_\infty = 1.64 \times 10^6$ m^{-1} and $U_\infty/\nu_\infty = 6.56 \times 10^6$ m^{-1} were obtained by varying the tunnel stagnation pressure (See Table 1).

U_∞/ν_∞ (m^{-1})	$\mathrm{Re}_x = U_e x/\nu_e$	$U_e/2\delta$ (kHz)
1.64×10^6	2.3×10^6	79
3.28×10^6	4.6×10^6	94
3.94×10^6	5.5×10^6	101
4.92×10^6	6.8×10^6	124
6.56×10^6	9.1×10^6	74

Table 1: Unit Reynolds number in freestream and length Reynolds number based on boundary layer edge conditions and a reference distance along the model surface of $x = 895$ mm.

The experimental model was a 7° half-angle cone, originally designed for Stetson et al. [20]. The cone is 1.016 m long, with a 250 mm base diameter. Although a number of interchangeable nose sections are available for use with this model, the present study used only a sharp nose with a spherical radius of 38 μm. The model was tested under near-adiabatic wall conditions.

The wind tunnel model and the coordinate systems used in the present paper are illustrated in Figure 1. The coordinates (x', y', z') are Cartesian, and oriented along the wind tunnel freestream, the vertical, and the spanwise directions, respectively. The coordinates (x, y, z) are an orthogonal curvilinear system aligned with the radial direction on the surface of the cone, the normal to the cone surface, and the circumferential direction.

The primary flow measurements were made using custom-built hot-film probes operated in constant-current mode. Up to three channels of data were obtained simultaneously, band-pass filtered between 10 Hz and 500 kHz, and recorded using a Bell and Howell model VR3700B analog FM tape recorder. The data were later digitized from the FM tapes using a CAMAC data acquisition system from Kinetic Systems, Inc., and stored on a Pentium PC for analysis. The two or three channels of data were digitized simultaneously at an effective sampling rate of 1.0 MHz in records of $2^{21} = 2097152$ contiguous samples per channel.[1] The software for controlling the CAMAC crate and analyzing the data was written by the authors in the C++ and FORTRAN 77 programming languages; most of the data analysis algorithms were adapted from the book by Bendat and Piersol [21].

Two probe drive mechanisms were available for po-

[1] For convenience, the tape was typically replayed at half-speed and sampled at 500 kHz.

sitioning the hot-film probes in the wind tunnel. An overhead probe drive, which could be retracted into an air lock above the test section, allowed motion of the probe mount along the vertical (y') and streamwise (x') directions. An on-board probe drive mounted on the model sting provided motion normal to the model centerline, while rolling the model allowed probe displacements along the circumferential (z) direction. In order to reduce the interference of the strut holding the on-board probe with the flow over the cone, a frustum was added to the basic cone model, with a slot to accommodate the probe mount. The frustum had the same 7° half-angle as the original model, and increased the size of the model to a length of 1.283 m with a base diameter of 315 mm.

Experiments involving circumferential probe separations were carried out using a single probe mounted on the on-board probe drive and a rake of up to four additional probes mounted on the overhead probe drive. The x' location of all the probes was held fixed at a location 889 mm downstream of the tip of the cone (x = 896 mm), and the y' location was fixed at that position in the boundary layer where maximum signal energy was recorded. Different circumferential separations between the probes were obtained by rolling the model, and thus the on-board probe, away from the rake.

Streamwise probe separations were obtained using a similar configuration. The on-board probe was held fixed at x' = 889 mm (x = 896 mm) at the y' location of maximum signal energy. The rake was held at a fixed circumferential separation from the on-board probe (ξ_z = 6.35 mm between the two nearest probes), but shifted to different downstream locations using the overhead drive. At each streamwise station, the rake of probes was relocated to the y' station of maximum signal energy.

An additional set of experiments was carried out with a pair of hot-film probes mounted on the rake with a fixed vertical separation of ξ_y = 1.47 mm. This pair of probes was traversed along the y' direction though the boundary layer with the overhead probe drive.

3 Results

3.1 General Character of Signal

Sound radiation from the turbulent boundary layers on the tunnel side-walls is believed to be the primary source of disturbances driving transition for experiments in conventional supersonic and hypersonic wind tunnels [22]. For compressible flow, linear stability theory [8, 10] predicts that boundary layer disturbances will be amplified in two frequency ranges, corresponding to the first and second modes. Measurements in the freestream of AEDC VKGDF Tunnel B [22] indicate that most of the energy content of the tunnel background noise is concentrated in a frequency range much lower than the characteristic frequency of the second mode instability ($f \sim U_e/2\delta$). In experimental data one would thus expect to see a second mode component arising from this 'quiet' frequency range, a relatively lower frequency first mode component driven by the tunnel background noise, and a modulation arising from the random nature of the tunnel noise.

Figure 2 shows sample time-series plots at Reynolds numbers Re_x of 2.3×10^6, 4.6×10^6, 6.8×10^6, and 9.1×10^6. These data were obtained at the value of y'/δ where the highest signal energy was detected. The streamwise station was held constant at x = 896 mm, and the Reynolds number was varied by changing the tunnel stagnation pressure.

The lowest Reynolds number case (Figure 2a) shows the expected wave-packet character. There is a dominant periodic component in the signal with a relatively low frequency modulation, and relatively quiescent periods alternate with packets of high-amplitude fluctuations. At a somewhat higher Reynolds number (Figure 2b), the quiescent periods are less frequent and the packets more prominant. As the Reynolds number is increased still further, the signals acquire a less regular character (Figures 2c and 2d), although some of the features of the initial instability are still detectable even at the highest Reynolds number.

Plots of the corresponding power spectral densities are shown in Figure 3. The two lower Reynolds number cases (Figures 3a and 3b) are dominated by a strong peak at the characteristic second mode frequency. Weak harmonics of this frequency are also evident in the plots, possibly indicating the initial onset of non-linearity in the transition process. There is suprisingly little energy content in the frequency range below the second mode. For higher values of the Reynolds number, the disturbance energy begins to be distributed over a range of frequencies (Figure 3c), and eventually the instability breaks down into turbulence (Figure 3d).

Figures 4 and 5 show, respectively, time-series plots and probability density functions for four different stations in the boundary layer at a Reynolds number of $\mathrm{Re}_x = 4.6 \times 10^6$. For the lowest station shown (Figure 4a), the most striking features are high-amplitude, predominantly negative 'spikes' in the signal. The probability density function (Figure 5a) shows a corresponding negative skewness. Higher in the boundary layer (Figures 4b and 5b), the negative spikes become more frequent, and the negative skewness of the PDF becomes quite striking.

Between $y'/\delta = 0.76$ and $y'/\delta = 0.78$ there is a qualitative change in the behavior of the signal: the negative tail on the PDF is balanced by a positive tail (Figure 5c) and both positive and negative 'spikes' are seen in the

time series plots (Figure 4c). The highest intensity of fluctuations are detected in the vicinity of this change in behavior. (The maximum signal energy occurs at $y'/\delta = 0.78 \pm 0.02$.) Still farther from the wall (Figures 4d and 5d), the PDF fills out, eventually forming a symmetric, Gaussian distribution.

In summary, the single-point time-series data are dominated by the second mode instability. The signals are intermittent, consisting of a random modulation imposed on a periodic signal. Power spectra are dominated by a peak at the characteristic frequency of the second mode, with surprisingly little energy at lower frequency, where wind tunnel background noise would be expected to drive the first mode. A qualitative change in the signal behavior was observed across the y'/δ station of maximum energy, presumably corresponding to the critical layer.

3.2 Disturbance Wave Orientation

One interesting aspect of the disturbance structure is the orientation in a surface parallel to the wall (x-z) represented by the skewness angle ψ. Over a range of supersonic and hypersonic Mach numbers, linear stability theory predicts that the most unstable second mode disturbance is oriented normal to the freestream ($\psi = 0$), and that the most unstable first mode disturbance is skewed to the freestream direction ($45° \leq \psi \leq 65°$ over $1 < \mathrm{Ma} < 10$). Wave skewness was investigated experimentally by acquiring data from probes with a circumferential separation (ξ_z).

Figure 6 shows an example of the broad-band cross-correlation for a Reynolds number of $\mathrm{Re}_x = 4.6 \times 10^6$. The cross-correlation displays a periodic component with a time scale characteristic of the second mode instability and a larger scale decay in time reflecting the limited streamwise coherence of the disturbance wave packets in the flow. If skewed waves were present in the flow, a pair of extrema, symmetric about zero time delay, would be expected in the cross-correlations. For a convection velocity of $0.9U_e \approx 41000$ in/s, a probe separation of $\xi_z = 0.5$ in, and a wave angle of $\phi = \pi/4$, there should be maxima at time delays of $\tau \approx \pm\ 12\ \mu$s. Instead, the optimal correlation occurs at zero time delay for the present case as well as for the other Reynolds numbers for which data is available (not shown).

The skewness of the different disturbance modes may not be apparent in the cross-correlation because it contains no frequency-dependent information about the signals – the skewness may 'wash out' in the calculation. An alternate way of looking at the two signals is through the cross-spectrum. Plots of coherence (e.g., Figure 7) do show that the signals have frequency-dependent features: a low-frequency component that may be related to the first mode and/or wind tunnel noise, the second mode, and the first harmonic of the second mode.

If, over a range of frequencies, there were a constant time shift τ between the two signals, we would expect to see a linear segment with slope $2\pi\tau$ in a plot of the phase versus frequency. Figure 8 shows the phase of the cross-spectrum for the $\mathrm{Re}_x = 4.6 \times 10^6$ case. Surprisingly, there is no time delay detectable in the data.

To examine the possibility that the instantaneous orientation of the boundary layer disturbances was different from the esemble-averaged orientation, the probability density function (PDF) of the phase of the cross-spectrum was computed. The phase PDF was computed by dividing each pair of contiguous records into windows of $2^6 = 64$ points[2], computing the cross-spectrum and its phase for each pair of windows, and incrementing a two dimensional array with indices corresponding to the phase and the frequency. For the present circumferential probe separation, a bimodal distribution of the phase would be expected if skewed waves were present in the flow.

Figure 9 shows the PDF of the phase for a Reynolds number of $Re_x = 2.3 \times 10^6$, plotted with frequency as a parameter. In this figure the horizontal axis corresponds to frequency in Hertz, the vertical axis corresponds to the phase, which ranges from $-\pi$ to π, and the contours correspond to the probability density. At the higher frequencies, there is essentially a uniform distribution of phase, as would be expected for uncorrelated noise. In the vicinity of the second mode frequency, however, there is a clear peak evident in the distribution of phase, centered near zero. A second peak is apparent at lower frequency.

Figure 10 shows the corresponding results for a Reynolds number of $Re_x = 4.6 \times 10^6$. Again, a uniform distribution of phase is observed for relatively high frequency, and a distribution peaked near zero phase is seen in the vicinity of the second mode frequency. The low-frequency peak apparent in the previous case is also present here. The major difference between the two cases is that for the high Reynolds number case the distribution is broader in the second mode frequency range and there is more separation in frequency between the second mode and the low-frequency component of the data.

These results are consistent with two-dimensional waves travelling in the direction of the freestream: each crest or trough of such a horizontal wave would intersect both hot-film probes simultaneously, creating no phase difference in the two signals. There is no evidence of oblique waves in the data.

[2]The window size was selected to correspond approximately to the characteristic time scale of the autocorrelation.

4 Conclusions

Two-dimensional, second-mode waves were detected in the Mach 8 flow over a 7° half-angle cone studied in the present project. No evidence of the first mode was found: little energy was detected in the lower frequency range, and no evidence of wave skewness was apparent.

According to stability theory [8, 9], the amplification of a boundary layer disturbance is very history-dependent in compressible flow. As a disturbance of constant frequency travels downstream in a compressible boundary layer, it is first amplified in the region of first mode instability, and farther downstream is amplified in the region of second mode instability. If disturbances originate at different streamwise stations (Reynolds numbers), as would be expected in a wind tunnel with background noise, early first mode growth might be averaged out by second mode amplification of disturbances originating farther downstream.

The problem with conventional transition experiments is that the origin – in space and time – of the disturbances entering the boundary layer is not known, so that it is not possible to examine a disturbance at a known stage in its amplification history. This question could be resolved by carrying out an experiment in a hypersonic flow similar to the experiment of Gaster and Grant [3], in which a localized, short-duration disturbance was introduced into an incompressible boundary layer, and synchonized measurements were made downstream.

References

[1] G. B. Schubauer and H. K. Skramstad. Laminar boundary layer oscillations and stability of laminar flow. *Journal of the Aeronautical Sciences*, 14:69–78, 1947. Originally published as confidential wartime report, April, 1943.

[2] J. L. Potter and J. D. Whitfield. Boundary layer transition under hypersonic conditions. AGARDograph 97, NATO Advisory Group for Aerospace Research and Development, 7 Rue Ancelle 92200 Neuilly Sur Seine France, 1965.

[3] M. Gaster and I. Grant. An experimental investigation of the formation and development of a wave packet in a laminar boundary layer. *Proceedings of the Royal Society of London A*, 347:253–269, 1975.

[4] M. Gaster. A theoretical model of a wave packet in the boundary layer on a flat plate. *Proceedings of the Royal Society of London A*, 347:271–289, 1975.

[5] J. Cohen, K. S. Breuer, and J. H. Haritonidis. On the evolution of a wave packet in a laminar boundary layer. *Journal of Fluid Mechanics*, 225:575–606, 1991.

[6] J. Cohen. The initial evolution of a wave packet in a laminar boundary layer. *Physics of Fluids*, 6(3):1133–1143, March 1994.

[7] W. O. Criminale and L. S. G. Kovasznay. The growth of localized disturbances in a laminar boundary layer. *Journal of Fluid Mechanics*, 14:59–80, 1962.

[8] L. M. Mack. Linear stability theory and the problem of supersonic boundary layer transition. *AIAA Journal*, 13(3):278–289, March 1975.

[9] C. D. Pruett and C.-L. Chang. Spatial direct numerical simulation of high-speed boundary-layer flows, part II: Transition on a cone in Mach 8 flow. *Theoretical and Computational Fluid Dynamics*, 7(5):397–424, 1995.

[10] L. M. Mack. Special course on stability and transition of laminar flow, sec. 3: Boundary-layer linear stability theory. AGARD Report AGARD-R-709, NATO Advisory Group for Aerospace Research and Development, 7 Rue Ancelle 92200 Neuilly Sur Seine France, 1984.

[11] L. D. Landau and E. M. Lifshitz. *Fluid Mechanics*. Pergamon Press, London, 1st edition, 1959.

[12] G. B. Whitham. A note on group velocity. *Journal of Fluid Mechanics*, 9:347–352, 1960.

[13] L. A. Segel. *Mathematics Applied to Continuum Mechanics*. Dover, New York, 1987.

[14] M. Van Dyke. *An Album of Fluid Motion*, chapter 5. The Parabolic Press, Stanford, CA, 1982.

[15] J. M. Kendall. Wind tunnel experiments relating to supersonic and hypersonic boundary-layer transition. *AIAA Journal*, 13(3):290–299, March 1975.

[16] T. B. Benjamin. The development of three-dimensional disturbances in an unstable film of liquid flowing down and inclined plane. *Journal of Fluid Mechanics*, 10:401–419, 1961.

[17] R. L. Kimmel, A. Demetriades, and J. Donaldson. Space-time correlation measurements in a hypersonic transitional boundary layer. AIAA Paper 95-2292, American Institute of Aeronautics and Astronautics, 1801 Alexander Bell Drive, Suite 500, Reston, VA 22091, June 1995.

[18] R. L. Kimmel and J. Poggie. Disturbance evolution and breakdown to turbulence in a hypersonic boundary layer: Ensemble-averaged structure. AIAA Paper 97-0555, American Institute of Aeronautics and Astronautics, 1801 Alexander Bell Drive, Suite 500, Reston, VA 22091, January 1997.

[19] Arnold Engineering Development Center. von Karman gas dynamics facility, vol. 3. Test facilities handbook, 11th ed., Arnold Engineering Development Center, April 1981.

[20] K. F. Stetson, E. R. Thompson, J. C. Donaldson, and L. G. Siler. Laminar boundary layer stability experiments on a cone at Mach 8, part 1: Sharp cone. AIAA Paper 83-1761, American Institute of Aeronautics and Astronautics, 1801 Alexander Bell Drive, Suite 500, Reston, VA 22091, July 1983.

[21] J. S. Bendat and A. G. Piersol. *Random Data: Analysis and Measurement Procedures.* J. Wiley, New York, 2nd edition, 1986.

[22] K. F. Stetson and R. L. Kimmel. On hypersonic boundary-layer stability. AIAA Paper 92-0737, American Institute of Aeronautics and Astronautics, 1801 Alexander Bell Drive, Suite 500, Reston, VA 22091, January 1992.

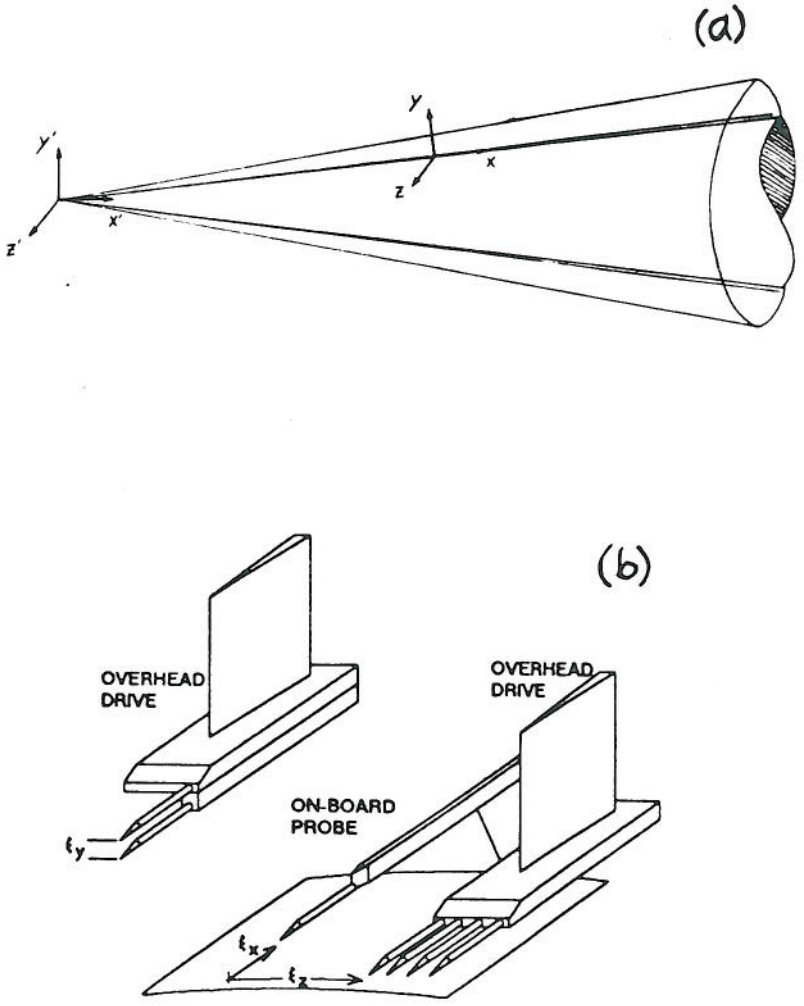

Figure 1: Experimental configuration. (a) Model and coordinate system. (b) Hot-film probe configuration.

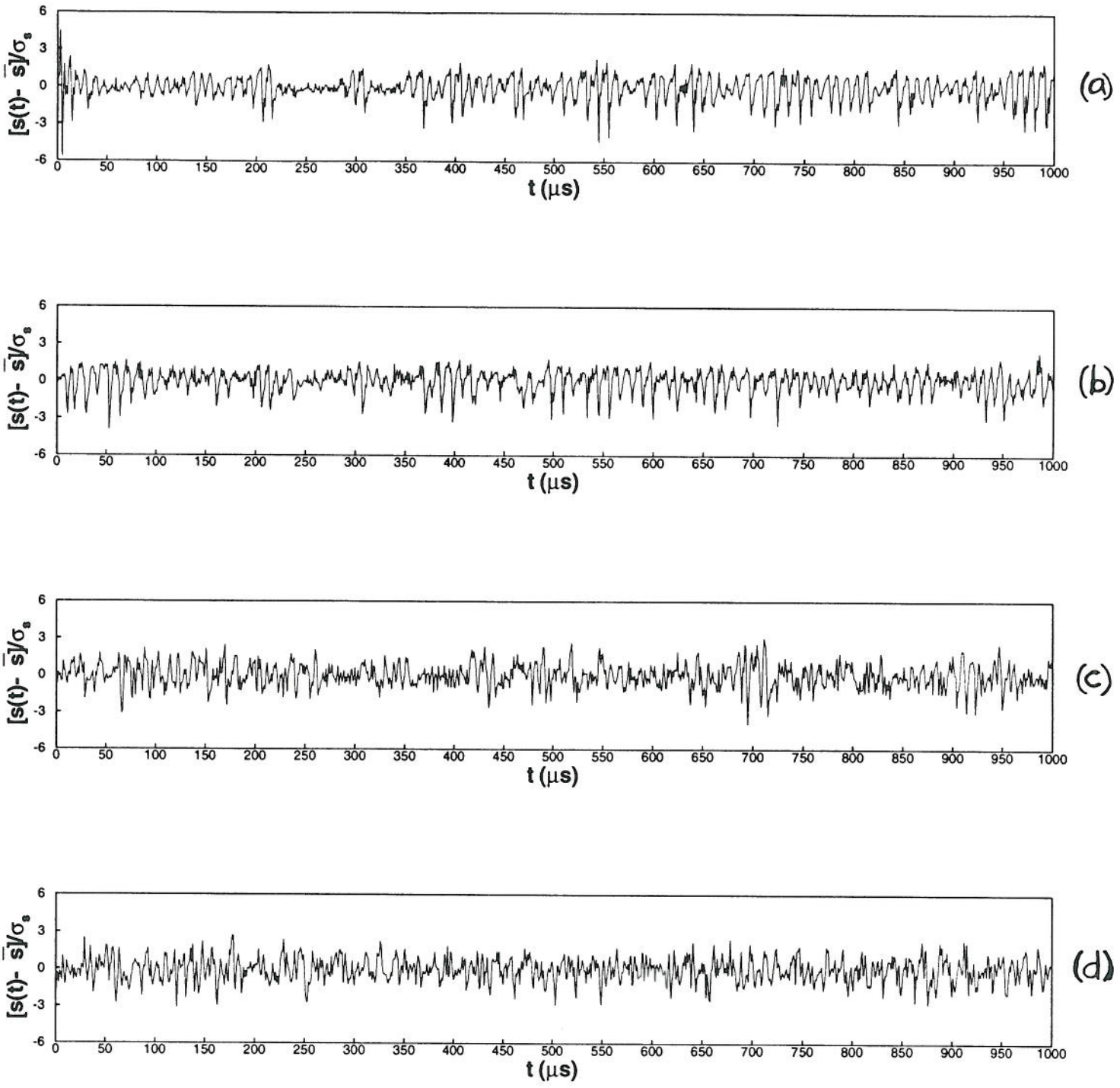

Figure 2: Time-series plots of the hot-film signal at the maximum energy station. (a) $\mathrm{Re}_x = 2.3 \times 10^6$. (b) $\mathrm{Re}_x = 4.6 \times 10^6$. (c) $\mathrm{Re}_x = 6.8 \times 10^6$. (d) $\mathrm{Re}_x = 9.1 \times 10^6$.

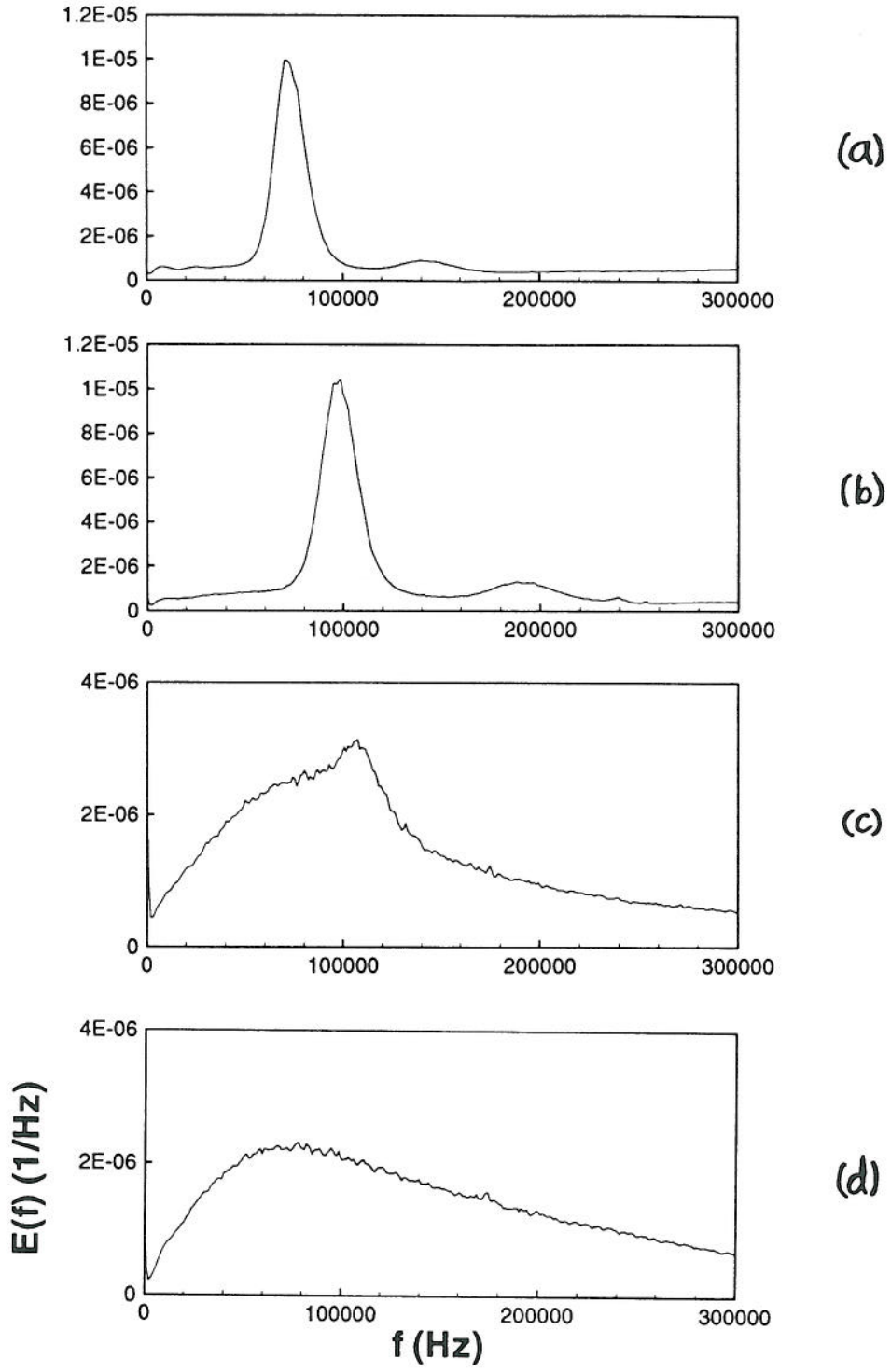

Figure 3: Power spectra at the maximum energy station. (a) $\mathrm{Re}_x = 2.3 \times 10^6$. (b) $\mathrm{Re}_x = 4.6 \times 10^6$. (c) $\mathrm{Re}_x = 6.8 \times 10^6$. (d) $\mathrm{Re}_x = 9.1 \times 10^6$.

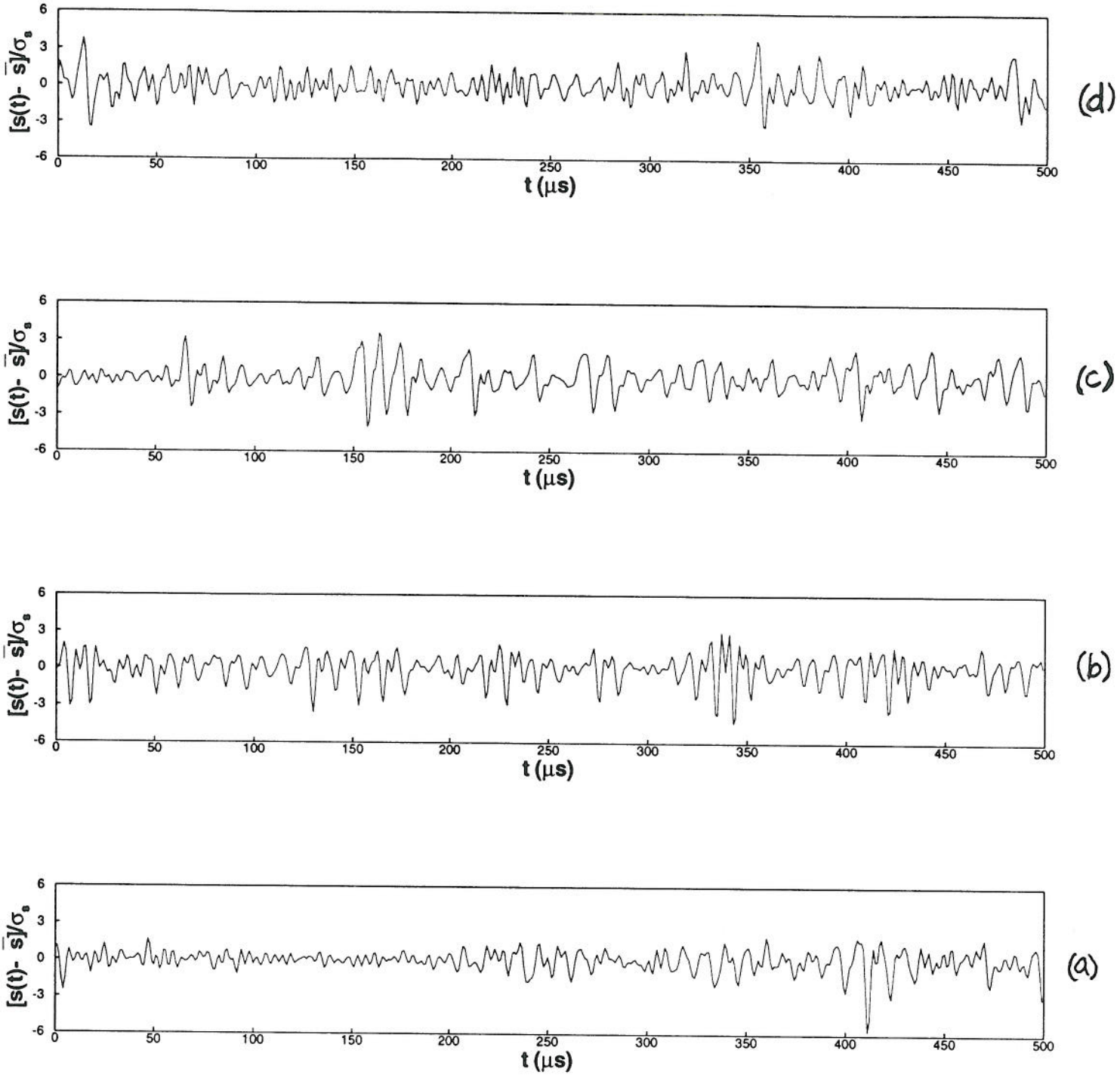

Figure 4: Time series plots for four stations across the boundary layer at $\mathrm{Re}_x = 4.6 \times 10^6$. (a) $y'/\delta = 0.64$. (b) $y'/\delta = 0.76$. (c) $y'/\delta = 0.78$. (d) $y'/\delta = 0.86$.

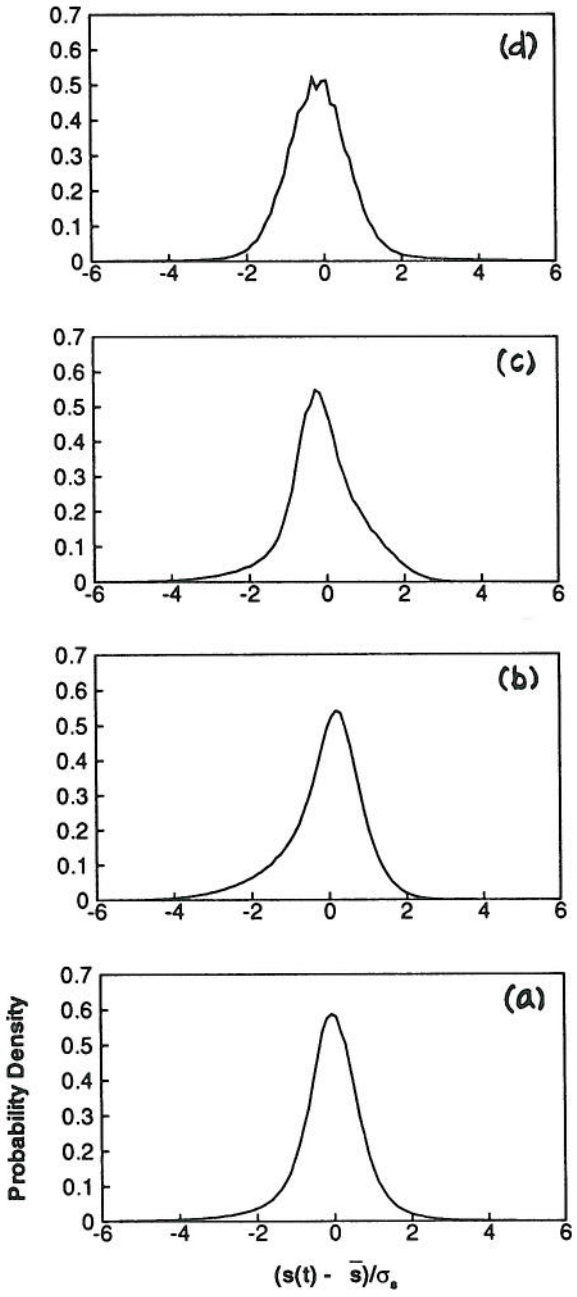

Figure 5: Probability density functions for four stations across the boundary layer at $\mathrm{Re}_x = 4.6 \times 10^6$. (a) $y'/\delta = 0.64$. (b) $y'/\delta = 0.76$. (c) $y'/\delta = 0.78$. (d) $y'/\delta = 0.86$.

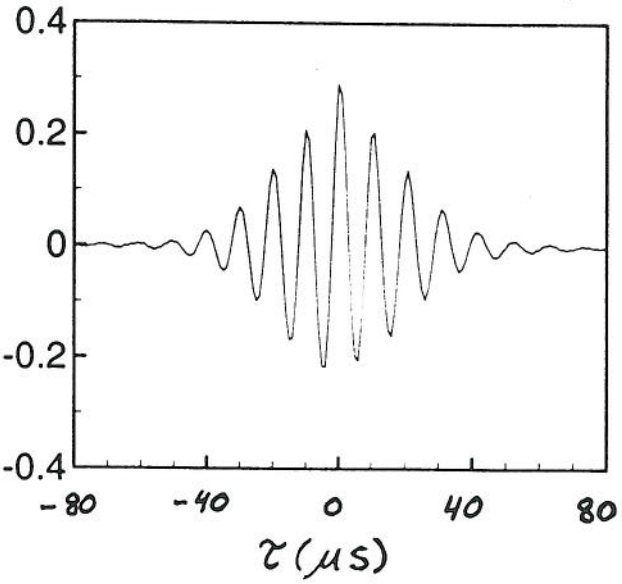

Figure 6: Broad-band cross-correlation for $\mathrm{Re}_x = 4.6 \times 10^6$ and $\xi_z/\delta = 2.1$.

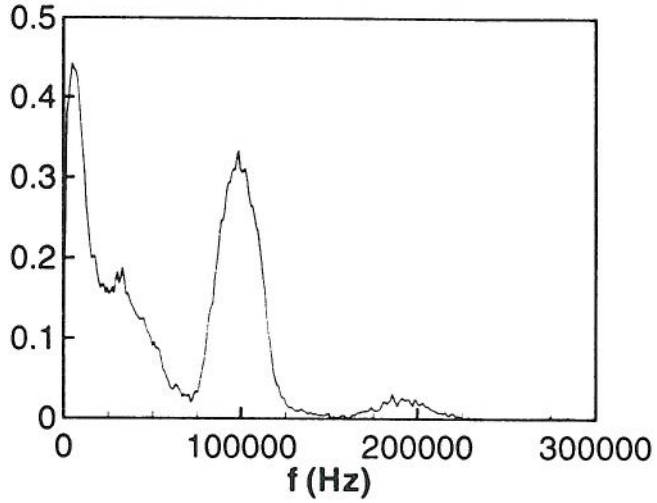

Figure 7: Coherence derived from the cross-spectrum for $\mathrm{Re}_x = 4.6 \times 10^6$ and $\xi_z/\delta = 2.1$.

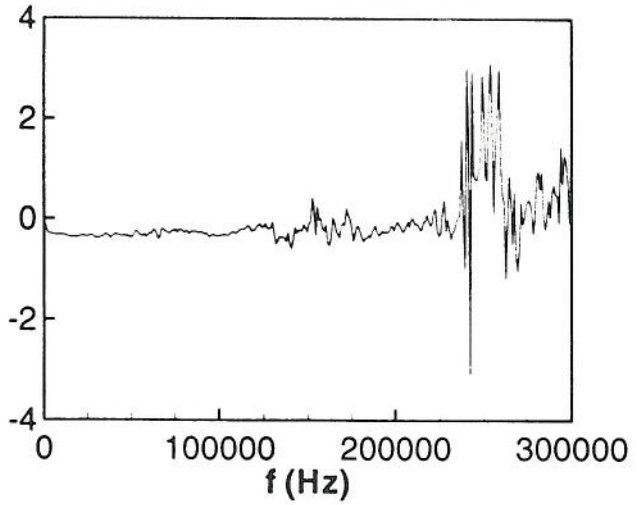

Figure 8: Phase of the cross-spectrum for $\mathrm{Re}_x = 4.6 \times 10^6$ and $\xi_z/\delta = 2.1$.

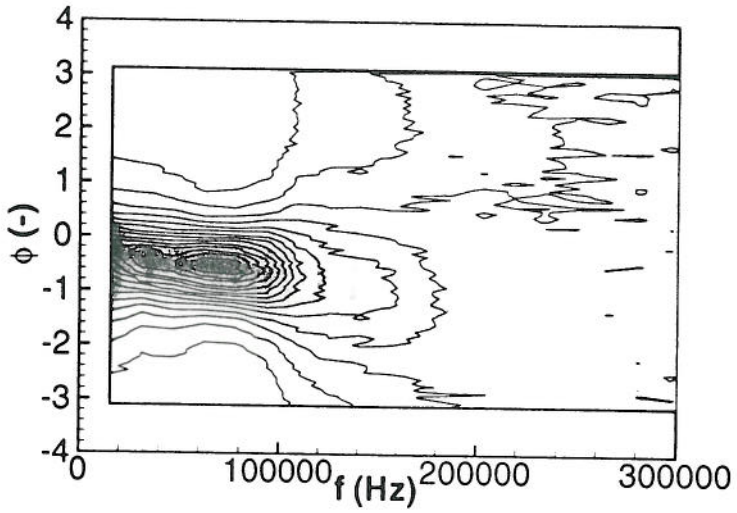

Figure 9: PDF of the phase as a function of frequency for $Re_x = 2.3 \times 10^6$ and $\xi_z/\delta = 1.3$. Contour interval 0.05.

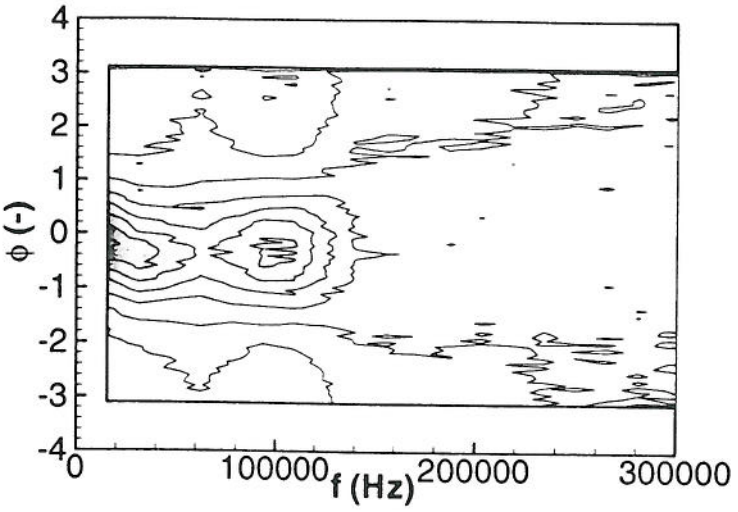

Figure 10: PDF of the phase as a function of frequency for $Re_x = 4.6 \times 10^6$ and $\xi_z/\delta = 2.1$. Contour interval 0.05.